Agricultural and Forest Meteorology 209–210 (2015) 100–113

Contents lists available at ScienceDirect

Agricultural and Forest Meteorology

journal homepage: www.elsevier.com/locate/agrformet

Terrestrial lidar remote sensing of forests: Maximum likelihood estimates of canopy profile, leaf area index, and leaf angle distribution

Kaiguang Zhao[a,*], Mariano García[b], Shu Liu[a], Qinghua Guo[c], Gang Chen[d], Xuesong Zhang[e], Yuyu Zhou[e], Xuelian Meng[f]

[a] School of Environment and Natural Resources, Ohio Agricultural and Research Development Center, The Ohio State University, Wooster, OH 44691, USA
[b] Center for Spatial Technologies and Remote Sensing, University of California at Davis, Davis, CA 95616, USA
[c] School of Engineering, University of California at Merced, Merced, CA 95343, USA
[d] Department of Geography and Earth Sciences, University of North Carolina at Charlotte, Charlotte, NC 28223, USA
[e] Joint Global Change Research Institute, Pacific Northwest National Laboratory and University of Maryland, College Park, MD 20740, USA
[f] Department of Geography and Anthropology, Louisiana State University, Baton Rouge, LA 70803, USA

ARTICLE INFO

Article history:
Received 7 November 2014
Received in revised form 7 March 2015
Accepted 14 March 2015
Available online 21 May 2015

Keywords:
LAI
Forest canopy
Leaf angle distribution
Terrestrial laser scanning
Ground-based lidar
Uncertainty analysis

ABSTRACT

Terrestrial laser scanning (TLS) swings a tiny-footprint laser to resolve 3D structures rapidly and precisely, affording new opportunities for ecosystem studies, but its actual utility depends largely on efficacies of lidar analysis methods. To improve characterizing forest canopies with TLS, we forged a methodological paradigm that combines physics and statistics to derive foliage profile, leaf area index (LAI), and leaf angle distribution (LAD): We modeled laser–vegetation interactions probabilistically and then developed a maximum likelihood estimator (MLE) of vegetation parameters. Unlike classical gap-based algorithms, MLE explicitly accommodates laser scanning geometries, fully leverages raw laser ranging data, and simultaneously derives foliage profile and LAD. We evaluated MLE using both synthetic lidar data and real TLS scans at sites in Everglades National Park, USA. Estimated LAI differed between algorithms by an average of 26%. Compared to classical gap analyses, MLE derived foliage density profile and LAD more accurately. Also, MLE has a rigorous statistical foundation and generated error intervals better indicative of the true uncertainties of estimated canopy parameters—an aspect often overlooked but essential for credible use of lidar vegetation products. The theoretical justification and experimental evidence converge to suggest that classical gap methods are sub-optimal for exploiting tiny-footprint lidar data and MLE offers a paradigm-shifting alternative. We envision that MLE will further boost confident use of terrestrial lidar as a versatile tool for environmental applications, such as forest survey, ecological conservation, and ecosystem management.

1. Introduction

Demands for reliable ecosystem structure data are growing in such fields as carbon sciences (Popescu et al., 2011), biometeorology (Chen et al., 2008), climate changes (Zhao and Jackson, 2014), wildlife and conservation ecology (Zellweger et al., 2014), ecosystem management (Hurtt et al., 2004), and fire ecology (Mutlu et al., 2008). Acquiring these data has long been pursued via conventional field and remote sensing techniques, such as hemispherical photography, multispectral imaging, and radar, yet with limited successes (Lefsky et al., 2002). A superior alternative being extensively explored during the passing decade is lidar—a suite of laser-based tools valuable for measuring 3D vegetation structure across spatial scales. The superiority of lidar was proven by a preponderance of empirical studies, thereby encouraging its further use. Indeed, lidar recently saw a surge in use by public and private sectors for land and ecosystem management (Vierling et al., 2008).

Numerous lidars have been deployed to measure terrestrial environments across scales, especially forest ecosystems (Richardson et al., 2009; Yu et al., 2011). Examples of the measured vegetation characteristics include, at tree levels, height, crown width, diameter at breast height, and crown base height (Dalponte et al., 2011; Lin et al., 2011; Popescu and Zhao, 2008), and at plot/stand levels, timber volume, biomass and carbon content, leaf area index (LAI), and canopy fuel parameters (García et al., 2012; Tang et al., 2014; van Aardt et al., 2006). These lidar

* Corresponding author. Tel.: +1 3302633722.
E-mail address: zhao.1423@osu.edu (K. Zhao).

http://dx.doi.org/10.1016/j.agrformet.2015.03.008
0168-1923/

systems differ in footprint, platform, data-recording, or operating mode. To date, the systems common to ecosystem studies are large-footprint spaceborne waveform profiler, small-footprint airborne discrete-return scanner, and tiny-footprint terrestrial discrete-return scanner. They cover a decreasing spatial extent but measure an increasing level of details.

Of current lidar technologies, terrestrial laser scanning (TLS), which is also known as ground-based or terrestrial lidar, delivers the finest characterization of forest structure (Hosoi and Omasa, 2006). The level of details acquired is unprecedented, with tree trunks, branches, twigs, or even leaves easily discernible. This high-resolution capability affords many exciting opportunities for vegetation research. As examples, tree diameters can be directly obtained from 3D TLS point clouds (Liang et al., 2012); efforts were also dedicated to delineating tree components from point clouds using automatic computer algorithms, with some promising results reported (Hosoi et al., 2013). The fine-grained measurements make TLS one of the best remote sensing tools to derive 3D distributions of phytoelements and related biophysical quantities, such as foliage profile, clumping index, and LAI (Yao et al., 2011; Zhao et al., 2011a).

Despite its great advantages, the use of TLS or any other lidars for vegetation survey still faces practical challenges. Foremost, TLS samples forests only partially, attributable to the occlusion from nearer-range vegetative elements (Lovell et al., 2003). This incompleteness complicates delineating tree geometry, generally making it impossible to fully recover components of interest, such as trunks and branches. Although the difficulty can be alleviated by coalescing multiple scans, segmentation of terrestrial lidar data into objects of interest still remains challenging (Liang and Hyyppa, 2013). Moreover, the scanning geometry of TLS leads to a more frequent sampling of near-range objects than far-range objects, which, if not corrected, will bias the estimation of certain forest structural variables (Jupp et al., 2009); for instance, tree heights are typically underestimated (Lovell et al., 2003).

The practical utility of lidar or TLS for vegetation analyses depends on not just its technical capabilities but also the effectiveness of ad-hoc lidar analysis methods in converting raw data into meaningful information (Chen and Hay, 2011; Woodgate et al., 2015). Common methods fall into two groups: those directly involving ground-truthing vs. those not. The first group encompasses many empirical models previously calibrated to correlate lidar metrics with biophysical variables (Jakubowski et al., 2013); however, correlative models for one region or time are not always transferrable to another. In contrast, the second group of methods turns to physics, signal processing, and heuristic rules, such as radiative transfer theories (Ni-Meister et al., 2008) and computer geometry algorithms (Zheng et al., 2013). These methods manifest improved transferability, but their design and applicability are limited by the validity of assumptions involved and also by the availability of prior knowledge, computer algorithms, and physical models.

Physics on light–vegetation interaction is particularly conducive to lidar analyses (Jupp et al., 2009), but how to best apply physics remains unclear, with room left for improvement. In general, laser–canopy interactions are theoretically described using physical gap models, but these models, though being probabilistic in nature, were rarely applied to analyze laser ranging data in a true probabilistic manner. Rather, laser ranging is transformed into ratio metrics as gap fractions, from which to further derive LAI. This indirect use of lidar data is inefficient and suboptimal, with many weaknesses in algorithm implementation. For example, gap-based LAI algorithms will fail if gap fractions are near zero. These algorithms rarely estimated leaf angle distribution; neither did they make strict statistical inference with regard to the true underlying gap probability model, therefore, providing no or sometimes misleading uncertainty analyses. In stark contrast, direct use of lidar data at rawer levels carries more information into canopy characterization and facilitates the integration of data and physics. The superiority of such data-rich paradigm was exemplified in our physically-based scale-invariant and machine learning biomass models (Zhao et al., 2011b, 2009). Despite its great potential (Palace et al., 2015), this paradigm is still underappreciated.

This study aims to enhance the utility of terrestrial lidar for measuring forest structure. Our specific objective is to forge a new paradigm to analyze tiny-footprint TLS data for deriving foliage density profile and leaf angle distribution at plot levels. Our analyses are based on the same physical principle as has been used in literature—the Poisson gap model. But different inherently from earlier work, we explicitly treated this gap model as the probability mechanism in generating laser ranging data, thereby allowing us to estimate vegetation parameters via the maximum likelihood principle. Similar to our previous airborne lidar analyses (Zhao et al., 2011b, 2009), this maximum likelihood estimator (MLE) incorporates raw lidar data into inference and, thus, improves data use efficiency and estimation accuracy. Another salient feature of MLE is its rigorousness in quantifying uncertainty.

2. Theoretical background

Our lidar vegetation analyses rely on the combined use of physics and statistics (Fig. 1). To provide a theoretical basis, we next describe the Poisson gap model—a physical principle central to vegetation remote sensing and our proposed MLE analyses. We also review classical LAI algorithms currently employed to invert the Poisson gap model and highlight their weaknesses.

2.1. Light–vegetation interaction: the Poisson gap model

Light–vegetation interactions have been modeled predominantly in a probabilistic manner (Nilson, 1971). Canopies are depicted as horizontally homogenous turbid random media (Fig. 1) and are characterized by structure and geometry parameters: one about leaf amount and another about leaf orientation, as denoted by $\boldsymbol{\vartheta}_{\text{veg}} = \{L(z), G(\theta)\}$. These parameters together determine the probability of light passing through a canopy along zenith angle θ from a base height z_0 to height z without being intercepted (Fig. 2):

$$P_{\text{gap}}(\theta, z) = \exp\left[\frac{-G(\theta)L(z)}{\cos\theta}\right]. \quad (1)$$

Here, $z = 0$ is the ground level, and the base height $z_0 = h_{\text{sensor}}$ is set at the laser equipment (Fig. 2). This model is known as the Poisson gap model. It offers not just a theoretical basis for radiative transfer in canopies but also practical tools to interpret gap-related data, such as hemispheric photos, laser ranging, and foliage-line intercept data (Jonckheere et al., 2004). Below, we explained the two types of canopy parameters $\boldsymbol{\vartheta}_{\text{veg}}\left\{L(z), G\left(\theta\right)\right\}$ in Eq. (1).

First, the vegetation geometry parameter $G(\theta)$ is defined as the mean projection of a unit foliage area onto the plane perpendicular to a viewing direction θ. $G(\theta)$, known as the Ross–Nilson function, is a function of zenith angle θ. Moreover, $G(\theta)$ is determined completely by leaf normal distribution or leaf angle distribution $g(\theta)$, following the relationship in Eq. (A1) (Wang et al., 2007). The leaf angle distribution $g(\theta)$ denotes the relative fraction of leaves that have normals pointing along the zenith angle θ. Note that both $g(\theta)$ and $G(\theta)$ were assumed to be azimuthally symmetric, an assumption implicitly made in almost all previous studies as well as in this study. Because of the equivalence between $g(\theta)$ and $G(\theta)$ as in Eq. (A1), the two are used exchangeably in the rest of the paper.

Leaf angle distribution, $g(\theta)$ or $G(\theta)$, is often parameterized in pre-defined functional forms (Otto and Trautmann, 2008). The parameterization circumvents difficulties in fully specifying val-

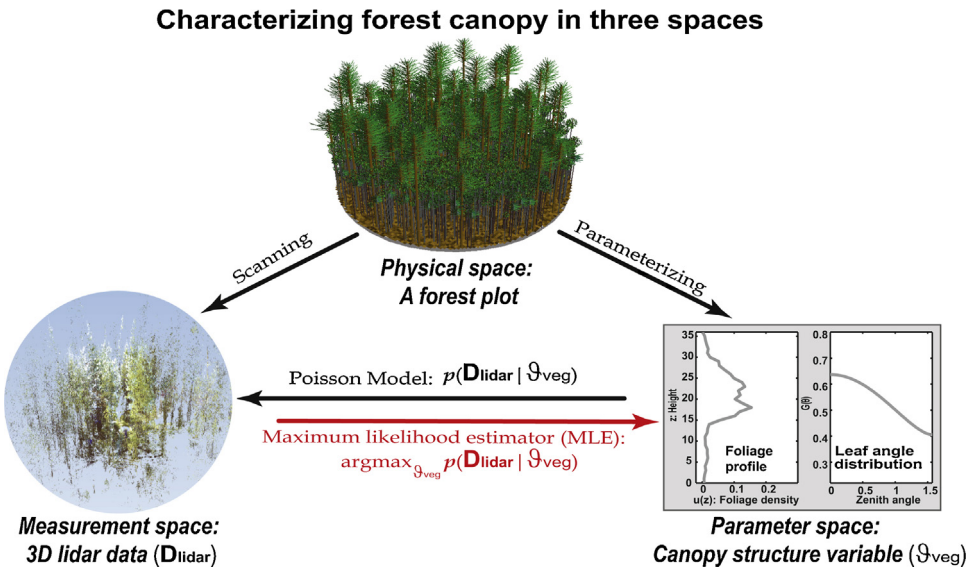

Fig. 1. A forest canopy in three contrasting yet linked spaces: Physical, measurement, and parameter. Their linkages are denoted by arrows. In particular, 3D laser data "D_{lidar}" are often linked to canopy parameters "$\boldsymbol{\vartheta}_{\text{veg}}$" through a physical model called the Poisson model $p\left(D_{\text{lidar}}|\boldsymbol{\vartheta}_{\text{veg}}\right)$. Our goal is to go from the measurement to parameter space for retrieving canopy parameters, such as foliage profile and leaf angle distribution, from laser data. The availability of the Poisson model as an underlying probability model makes the maximum likelihood estimator (MLE) a natural choice to directly estimate canopy parameters from 3D lidar data (see Section 3.1 for details).

ues of $g(\theta)$ or $G(\theta)$ pointwise for each zenith $\theta \in [0, \pi/2]$. Most parameterization schemes employ up to two parameters to determine the functional shape of $g\left(\theta; \chi\right)$ or $G(\theta\,; \chi)$ with χ being the parameters (Table 1). Several simple models, such as planophile, and erectophile models, are pre-defined equations with no specifying parameter. In contrast, the ellipsoid distribution, as in the HemiView software, requires only one parameter. Another common model for $g(\theta)$ is the beta distribution with two parameters, but its associated G-function $G(\theta)$ has no neatly analytical form. In this case, $G(\theta)$ should be numerically evaluated from $g(\theta)$ via Eq. (A1).

Second, the vegetation structural parameter $L(z)$ in the gap model denotes the cumulative leaf area from the reference height z_0 up to z, which is calculated by integrating the vertical profile of leaf area density $u(z)$:

$$L(z) = \int_{z_0}^{z} u\left(z'\right) \mathrm{d}z'. \tag{2}$$

More specifically, $u(z)$ is the leaf area per unit volume around a location at height z. The integration of foliage density profile $u(z)$ over the whole canopy layer from the ground up to the canopy height H gives the total leaf area per unit ground area, that is, LAI (Fig. 2). Because of the equivalence between $u(z)$ and $L(z)$, the two are used exchangeably in this paper.

Foliage area density or foliage profile $u(z)$ has been characterized both parametrically and non-parametrically. Common parametric models include the Weibull, the beta, and the Johnson SB distributions (Medhurst and Beadle, 2001; Mori and Hagihara, 1991; Yang et al., 1993). The Weibull model, for example, is parameterized by four scalars $[u_0, H, k,\ \upsilon]$ in the form of

$$u_{Weibull}\left(z|u_0, H, \kappa, \upsilon\right) = u_0 \times \frac{\kappa}{\upsilon}\left(\frac{H-z}{\upsilon}\right)^{\kappa-1} \times e^{-\left(\frac{H-z}{\upsilon}\right)^{\kappa}}. \tag{3}$$

As nonparametric alternatives, the curve of $u(z)$ can be specified at selected heights $\left\{z_j = j \times \Delta h\right\}_{j=1,\ldots,m}$, with Δh being a height bin size:

$$u\left(z\right) \xrightarrow{\text{discretize}} \left\{u_j = u\left(z_j\right) : z_j = j \times \Delta h\right\}_{j=1,\ldots,m}. \tag{4}$$

This discretized version $\{u_j\}_{j=1,\ldots,m}$ will capture more details in foliage profile with smaller bins Δh. Compared to the paramet-

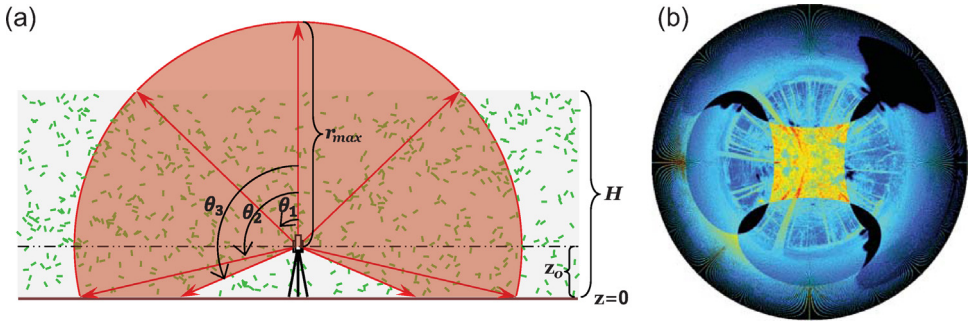

Fig. 2. (a) Schematic of terrestrial laser scanning (TLS) for a horizontal homogenous canopy of height H. The laser, placed at height z_0, scans the canopy up to a maximum range $r_{\max}$ from the nadir up to a maximum zenith angle θ_3. The ranging limit $r_{\max}$ and scan angle θ_3 are often customizable. The probability of laser intercepting phytoelements (e.g., leaf, twig, and branch) is often described by the Poisson model (Section 2). Notice that for a scanning zenith less than θ_1 = across$(H - z_0)/r_{\max}$, the laser can "see" through the top of the canopy, and when the angle reaches beyond θ_2 = across $z_0/r_{\max}$, the laser may hit the ground. This scanning geometry is difficult to consider by traditional methods when inverting the Poisson model to estimate LAI, but it can be easily accounted for by our MLE method. (b) An example of scanning pattern for a Riegel scanner is depicted in the hemispheric coordinate, where the black color indicates the blind zones not scanned and the color gradient indicates the sum of laser intensity.

Table 1
A list of 15 common parametric models for leaf angle distribution, as formulated for either leaf normal distribution $g(\theta)$ or Ross-Nilson geometry factor $G(\theta)$. $G(\theta)$ denotes the projection of a unit foliage area onto a plane perpendicular to the zenithal direction; $G(\theta)$ is determined inherently by $g(\theta)$ according to Eq. (A1). Shorthand for the models is noted in the "Acronym" column; the valid ranges of model parameters are given in the "Parameter" column.

Model Type	Acronym	Model equation of $g(\theta)$ or $G(\theta)$	Parameter
Uniform	uni	$g(\theta)=2/\pi$	NA
Spherical	sph	$g(\theta)=\sin\theta$	NA
Horizontal	hor	$G(\theta)=\cos\theta$	NA
Vertical	vtc	$G\left(\theta\right)=2/\pi\cdot\sin\theta$	NA
Erectophile	erc	$g\left(\theta\right)=2/\pi\cdot\left(1+\cos(2\theta)\right)$	NA
Planophile	pln	$g\left(\theta\right)=2/\pi\cdot\left(1-\cos(2\theta)\right)$	NA
Plagiophile (mainly around 45)	plg	$g\left(\theta\right)=2/\pi\cdot\left(1-\cos(4\theta)\right)$	NA
Extremophile (mainly erect or parallel)	ext	$g\left(\theta\right)=2/\pi\cdot\left(1+\cos(4\theta)\right)$	NA
Beta distribution	bet	$g\left(\theta;u,\upsilon\right)=\frac{2}{\pi}\frac{\Gamma(u+\upsilon)}{\Gamma(u)\Gamma(\upsilon)}\left(1-\frac{2\theta}{\pi}\right)^{u-1}\left(\frac{2\theta}{\pi}\right)^{\upsilon-1}$	$u,\upsilon>1$
Elliptical	elt	$\begin{cases} g(\theta;\epsilon,\theta_m)=\dfrac{\Delta}{\sqrt{1-\epsilon^2\cos^2(\theta-\theta_m)}} \\ \Delta=\epsilon/\left[\cos\theta_m\cdot\log\left(\dfrac{\cos\eta+\sin\upsilon}{\cos\upsilon-\cos\eta}\right)-\sin\theta_m\cdot(\eta-\upsilon)\right] \\ \eta=\sin^{-1}(\epsilon\cos\theta_m) \\ \upsilon=\sin^{-1}(\epsilon\sin\theta_m) \end{cases}$	$0\le\epsilon\le1$ $0\le\theta_m\le\dfrac{\pi}{2}$
Ross–Goudriann's model	r–g	$\begin{cases} G(\theta;\chi_L)=\varphi_1+\varphi_2\cos\theta \\ \varphi_1=0.5-0.633\chi_L-0.33\chi_L^2 \\ \varphi_2=0.877(1-2\varphi_1) \end{cases}$	$-0.4\le\chi_L\le0.6$
Dickinson's model	dks	$\begin{cases} G(\theta;\chi_L)=\varphi_1+\varphi_2\cos\theta \\ \varphi_1=0.5-0.489\chi_L-0.11\chi_L^2 \\ \varphi_2=1-2\varphi_1 \end{cases}$	$-1\le\chi_L\le1$
Ellipsoidal	els	$\begin{cases} G(\theta;x)=\dfrac{\sqrt{x^2\cos^2\theta+\sin^2\theta}}{x+1.702(x+1.12)^{-0.708}} \\ g(\theta;x)=2x^2\sin\theta/\left[\Lambda(\cos^2\theta+x^2\sin^2\theta)^2\right] \\ \Lambda=\begin{cases} 1+\dfrac{\log[(1+\epsilon_1)/(1-\epsilon_1)]}{2\epsilon_1x^2};\ \epsilon_1=\sqrt{1-x^{-2}},x>1 \\ 1+\dfrac{\sin^{-1}\epsilon_2}{x\epsilon_2};\qquad \epsilon_2=\sqrt{1-x^2},x<1 \end{cases} \end{cases}$	$x>0$
Jupp's model	jup	$G\left(\theta;x\right)=x\cos\theta+(1-x)\frac{2}{\pi}\sin\theta$	$0\le x\le1$
Lang's model	lan	$G\left(\theta;x\right)=(x+(1-x)\theta)/2$	$0\le x\le1$

ric models (e.g., Eq. (3)), the nonparametric representation is more flexible, especially if canopy vertical structures are too complex to be adequately approximated by parametric curves. However, this benefit comes at the expense of having many more unknowns to be specified (Zhao et al., 2009). For example, if specifying a profile with a 0.1-m bin up to 50 m, almost five hundred unknowns need to be determined (i.e., $m=500$), compared to only four unknown parameters in the Weibull model.

2.2. Classical LAI inversion algorithms

The Poisson gap model has long been inverted to retrieve canopy profiles and LAI from gap data (Jonckheere et al., 2004). Existing inversion algorithms fall roughly into three groups. First, in its simplest form, LAI can be estimated by re-writing Eq. (1) as

$$L(z)=-\frac{\cos\theta}{G(\theta)}\log P_{gap}(\theta,z). \tag{5}$$

This formula is of limited usefulness because the geometry factor $G(\theta)$ is often unknown. However, $G(\theta)$ for most canopies takes a relatively constant value of 0.5 near $\theta=57.5^\circ$, regardless of exact functional forms of $G(\theta)$. Therefore, gap fractions observed around this hinge angle 57.5°, $P_{\rm gap}(57.5^\circ,z)$, together with $G(57.5^\circ)\approx0.5$, can be plugged into Eq. (7) to get a rough estimate of $L(z)$. The estimated cumulative leaf area index $L(z)$ can then be differentiated with respect to height z to obtain foliage area density $u(z)=\partial L(z)/\partial z$.

The second group of algorithms is derived from the Miller's formula $\int_0^{\frac{\pi}{2}}G(\theta)\sin\theta{\rm d}\theta=\frac{1}{2}$ (Nilson, 1999; Zhao and Popescu, 2009), which, combined with Eq. (1), leads to

$$L(z)=-2\int_0^{\pi/2}\log\left[P_{gap}(\theta,z)\right]\cdot\cos\theta\sin\theta{\rm d}\theta. \tag{6}$$

This equation eliminates the dependence on the Ross–Nilson function $G(\theta)$ and tends to use gap fractions $P_{\rm gap}$ observed at all zenith angles, thus improving upon the simple algorithm in Eq. (5). In practice, the integration over $[0,\pi/2]$ in Eq. (6) is done numerically by summing over a few selected zenith annuluses (e.g., 7°, 23°, 38°, 53°, and 68° for Plant gap analyzer) (Rich et al., 1999).

Third, unlike the first two groups of algorithms, many other algorithms are devised by assuming certain functional forms for $G\left(\theta;\chi\right)$ with χ being some unknown parameters. The parameters χ together with LAI need to be estimated from data, typically using the least-square method. For example, Jupp et al. (2005) considered a G model $G\left(\theta;\chi\right)=\chi\cos\theta+(1-\chi)\frac{2}{\pi}\sin\theta$, which is a mixture of the vertical and horizontal leaf angle distributions with the mixing ratio χ as the unknown parameter (Table 1). Using this G model, Eq. (1) becomes

$$\underbrace{-\log P_{gap}(\theta,z)}_{\updownarrow\ \widehat{y}}=\underbrace{L(z)\cdot\chi}_{\updownarrow\ A}+\underbrace{L(z)\cdot(1-\chi)}_{\updownarrow\ B}\times\underbrace{2/\pi\cdot\tan\theta}_{\updownarrow\ x}. \tag{7}$$

The coefficients $A=L(z)\chi$ and $B=L(z)(1-\chi)$ can be estimated by regressing $y=-\log P_{\rm gap}(\theta,z)$ against $x=2/\pi\times\tan\theta$; then LAI is obtained as $\hat{L}(z)=\hat{A}+\hat{B}$. The same method was also proposed in Lang (1987) but using a slightly different G model. For ease of refer-

ence, we termed the algorithm of Eq. (7) as the Lang–Jupp method. Another common algorithm of this kind is the one for the HemiView software that adopts the ellipsoidal G model (Table 1). Its associated G parameter and the leaf area $L(z)$ are simultaneously inverted by minimizing the difference between the observed and modeled values of $-\log P_{\text{gap}}(\theta, z)$ (Campbell and Norman, 1989).

Despite seeing widespread use, these existing algorithms have practical limitations. For example, the simple hinge-angle algorithm is inefficient because of discarding gap observations at angles other than 57.5°. More important, all the algorithms may fail because evaluations of $\log P_{\text{gap}}\left(\theta, z\right)$ will cause errors if $P_{\text{gap}} \approx 0$. In addition, the algorithms in the third group implicitly assume some "wrong" statistical models that have error structures inconsistent with the true probability mechanism underlying the gap data, a subtle yet nontrivial limitation that has never been examined before. For example, linear regression adopted for Eq. (7) implicitly assumes homogeneous errors in the observed " $-\log P_{\text{gap}}\left(\theta, z\right)$ ", which is not always the case. All these limitations will be automatically dismissed by simply switching to a MLE paradigm, as detailed next.

3. Methods

Laser ranging data acquired with tiny-footprint lidar are often interpreted through the Poisson probabilistic model described above in Eq. (1). This direct involvement of probability model enables inferring vegetation parameters from laser ranging data with the maximum likelihood principle (Fig. 1). Specifically, recall that when a dataset D_{lidar} is observed from an underlying probability model $p\left(D_{\text{lidar}}|\boldsymbol{\vartheta}_{\text{veg}}\right)$ with $\boldsymbol{\vartheta}_{\text{veg}}$ being some fixed yet unknown parameters, a natural choice for inference is the maximum likelihood estimator (MLE) (Casella and Berger, 1990):

$$\hat{\boldsymbol{\vartheta}}_{\text{MLE}} = \arg\max_{\boldsymbol{\vartheta}_{\text{veg}}} p\left(D_{\text{lidar}}|\boldsymbol{\vartheta}_{\text{veg}}\right) \tag{8}$$

which seeks the particular value of $\boldsymbol{\vartheta}_{\text{veg}}$ that maximizes the probability of observing D_{lidar}. For clarification, $p\left(D_{\text{lidar}}|\boldsymbol{\vartheta}_{\text{veg}}\right)$ is known as a probability function of data D_{lidar} given the parameters $\boldsymbol{\vartheta}_{\text{veg}}$, but is a likelihood function of $\boldsymbol{\vartheta}_{\text{veg}}$ given the data D_{lidar}. Despite the widespread use of MLE in essentially all disciplines and a justifiable niche of MLE for analyzing gap or laser ranging data, we have not found any previous studies that explicitly considered MLE for such analyses. This lack of prior studies comes as a surprise to us, given the growing body of literature that uses gap probability models as the basic physics to analyze gap and laser ranging data.

Use of MLE to estimate vegetation parameters from lidar data is conceptually simple, but its detailed formulation inevitably involves some mathematics. In particular, we have to revise the original gap model Eq. (1) to model laser ranging rather than gaps (Sections 3.2–3.6). Readers not interested in technical specifics may skip directly to Section 4 for our lidar vegetation analysis and results; they may also go to the Appendix A2 for a quick example to learn the essence and advantages of MLE over classical LAI inversion algorithms. For those readers who are interested in the derivation but find it difficult, we recommend them to first glean some basic knowledge about MLE from introductory materials (e.g., Myung, 2003). Our MLE method was implemented in MATLAB®; the code can be requested from the primary author.

3.1. Lidar data characteristics

We begin to detail our MLE method by first highlighting some characteristics of TLS data, which is the data component D_{lidar} in the likelihood $p\left(D_{\text{lidar}}|\boldsymbol{\vartheta}_{\text{veg}}\right)$ (Figs. 1 and 2). Most commercial terrestrial lidars measure ranging, intensity, or even color RGB data, but only the ranging data are treated in our MLE method (Fig. 2).

Laser ranging data are commonly represented as a point cloud, either in the Cartesian $[x_i, y_i, z_i]_{i=1,\ldots,n}$ or spherical $[r_i, \theta_i, \phi_i]_{i=1,\ldots,n}$ coordinates (Fig. 2), but these representations fail to reveal the full information about laser–canopy interactions: The point cloud corresponds to only those laser shots that produce a hit. We therefore need to recover those shots that intercept nothing within the scanner's effective ranging limit $r_{\max}$ (Fig. 2). These missing shots produce no xyz returns and often are not saved in standard output files, but they are easily recoverable in an ad-hoc manner because the laser scans at a regular pattern. Following the scanning pattern, a sweep of the point cloud allows us to identify those scan directions along which the laser hits nothing, thus, uncovering the unrecorded laser shots. This functionality indeed is implemented in software programs for some commercial TLS (e.g., Leica Cyclone). Moreover, if the laser looks downward beyond a critical angle, returns may come from the ground rather than vegetation (Fig. 2). Such ground returns should be differentiated from vegetation returns.

The above pre-processing procedure converts the original TLS point cloud $[r_i, \theta_i, \phi_i]_{i=1,\ldots,n}$ into an augmented version of data D_{lidar} that is required for our MLE method:

$$\begin{aligned} D_{lidar} = & [r_i, \theta_i, \varphi_i, s_i = +1]_{i=1,\cdots,m} \\ & \cup [r_i = z_0/|\cos\theta_i|, \theta_i, \varphi_i, s_i = -1]_{i=m+1,\cdots,n} \\ & \cup [r_i = r_{\max}, \theta_i, \varphi_i, s_i = 0]_{i=n+1,\cdots,N} \end{aligned} \tag{9}$$

where lidar totally emits N shots, n of which produce returns, as indicated by the status variable $s_i = \pm 1$, and the other $N-n$ produce no returns (i.e., $s_i = 0$). For those n shots with returns, m of them hit phytoelements (i.e., $s_i = +1$) and the other $n-$m shots hit the ground (i.e., $s_i = -1$). In short, the full laser ranging data D_{lidar} is comprised of three subsets representing laser shots that hit vegetation ($s_i = +1$), the ground ($s_i = -1$), and nothing ($s_i = 0$), respectively. Note that in the following analyses, the azimuth ϕ_i of D_{lidar} was discarded because the azimuthal symmetry was assumed for canopies.

3.2. The Poisson model $p\left(D_{lidar}|\boldsymbol{\vartheta}_{veg}\right)$ for laser ranging

Raw lidar measurements are not gap fractions but ranging data. We, therefore re-formulated the gap model of Eq. (1) to instead calculate the interception probability that a laser shot hits phytoelements at height z along angle θ:

$$p_{\text{hit}}\left(\theta, z\right) = -\frac{\partial P_{\text{gap}}\left(\theta, z\right)}{\partial z} = \frac{1}{\cos\theta} G\left(\theta\right) u\left(z\right) \exp\left[\frac{-G(\theta)L(z)}{\cos\theta}\right]. \tag{10}$$

This equation is a probability distribution with respect to z: More strictly speaking, the probability of a shot hitting within a height bin Δz around z along θ is $p_{\text{hit}}(\theta, z) \times \Delta z$. If further expressed in the spherical coordinate, Eq. (10) gives the probability of a laser shot hitting vegetation at a distance r_i along θ_i:

$$p_{\text{hit}}\left(\theta_i, r_i\right) = G\left(\theta_i\right) \cdot u\left(r_i \cdot \cos\theta_i + z_0\right) \cdot \exp\left[\frac{-G\left(\theta_i\right) \cdot L\left(r_i \cdot \cos\theta_i + z_0\right)}{\cos\theta}\right] \tag{11}$$

where the origin of the spherical coordinate is situated at the scanner height $z_0 = h_{\text{sensor}}$ (note that $z = 0$ is the ground level). $p_{\text{hit}}(\theta_i, r_i)$ also represents the probability of observing a vegetation return $[r_i, \theta_i, \phi_i, s_i = +1]$.

In the case that a laser shot intercepts nothing or hits the ground (i.e., $[r_i = z_0/|\cos\theta_i|, \theta_i, \phi_i, s_i = -1]$ or $[r_i = r_{\max}, \theta_i, \phi_i, s_i = 0]$), the probability of such an event is equal to that of observing a gap when

seeing through the canopy from the scanner up to a distance of r_i:

$$p_{\text{miss}}\left(\theta_i, r_i\right) = 1 - \int_0^{r_i} p_{\text{hit}}\left(\theta_i, r\right) \mathrm{d}r = \exp\left[\frac{-G(\theta_i)L(r_i \cdot \cos\theta_i + z_0)}{\cos\theta_i}\right] \tag{12}$$

where r_i is equal to the scanner's ranging limit $r_{\max}$ if the shot hits nothing, but r_i is equal to $z_0/|\cos\theta_i|$ if the shot hits the ground (Fig. 2).

The expressions in Eqs. (11) and (12) combine to serve as the probability model $p\left(D_{\text{lidar}}|\boldsymbol{\vartheta}_{\text{veg}}\right)$ for the full data D_{lidar}, with Eq. (11) for the first subset of the D_{lidar} (i.e., $s_i = +1$: canopy returns) and Eq. (12) for the second and third subsets (i.e., $s_i = -1$ or $s_i = 0$: ground return or no returns). Noteworthily, this new version of Poisson model explicitly accounts for the scanning setting and geometry, such as scanner height, scanner zenith range, and ranging limit.

3.3. Maximum likelihood estimator (MLE)

Our MLE method assumes that lidar measures discrete-returns with a sufficiently-small footprint so that the Poisson model elicited above in Eqs. (11) and (12) is a reasonable approximation, an assumption that has been implicitly made in many early studies (Zheng et al., 2013). Using the observation probabilities $p_{\text{hit}}\left(\theta_i, r_i\right)$ and $p_{\text{miss}}\left(\theta_i, r_i\right)$ of Eqs. (11) and (12) for individual laser shots, we obtained the probability of observing the full lidar data D_{lidar} conditional on vegetation parameters $\boldsymbol{\vartheta}_{\text{veg}} = \left\{L(z), G(\theta)\right\}$, which is often expressed in the form of log-likelihood:

$$\begin{aligned}\mathcal{L}(\underbrace{G(\theta),\ u(z)}_{\vartheta_{\text{veg}}}|D_{\text{lidar}}) &= \log p\left(D_{\text{lidar}}|G\left(\theta\right),\ u(z)\right) \\ &= \sum_{i=1}^{n} \log p_{\text{hit}}\left(\theta_i,\ r_i\right) + \sum_{i=n+1}^{N} \log p_{\text{miss}}\left(\theta_i,\ r_i\right)\end{aligned} \tag{13}$$

Maximizing it with respect to the parameters $G(\theta)$ and $u(z)$ yields the MLE estimate:

$$\begin{aligned}\hat{\boldsymbol{\vartheta}}_{\text{veg}} &= \left\{\hat{G}_{\text{MLE}}\left(\theta\right),\ \hat{u}_{\text{MLE}}(z)\right\} \\ &= \underset{\left\{G(\theta),\, u(z)\right\}}{\arg\max}\ \mathcal{L}\left(G\left(\theta\right), u(z)|D_{\text{lidar}}\right).\end{aligned} \tag{14}$$

Despite being conceptually simple, the implementation of MLE may not be straightforward to some readers. We adopted several practical tricks for its efficient implementation. Foremost, the parameters of interest, $\boldsymbol{\vartheta}_{\text{veg}} = \left\{L(z), G(\theta)\right\}$, comprise not just a few scalars but are continuous functions over zenith angle θ and height z, respectively. To tackle this, we considered the parametric representation for leaf angle distribution $G(\theta)$ and the non-parametric representation for foliage profile $u(z)$, as detailed in Section 2.1. Other practical tricks for efficiently implementing Eq. (14) are supplied in the Appendix A.

3.4. Uncertainty analysis

MLE yields not just the best values of vegetation parameters but also error intervals. According to Casella and Berger (1990), the variance of our MLE estimate $\hat{\text{V}}\text{ar}\left(\hat{\boldsymbol{\vartheta}}_{\text{veg}}\right)$ can be derived by inverting the o bserved information matrix of the log-likelihood $\mathcal{L}\left(G\left(\theta\right), u(z)|D_{\text{lidar}}\right)$:

$$\hat{\text{V}}\text{ar}\left(\hat{\boldsymbol{\vartheta}}_{\text{veg}}\right) = I^{-1}\left(\hat{\boldsymbol{\vartheta}}_{\text{veg}}\right) = \left[\frac{\partial^2 \mathcal{L}}{\partial\vartheta_i \partial\vartheta_j}\Big|_{\hat{\boldsymbol{\vartheta}}_{\text{veg}}}\right]^{-1} \tag{15}$$

where ϑ_i and ϑ_j denote the i-th and j-th scalar parameters in the vector $\boldsymbol{\vartheta}_{\text{veg}}$. The availability of this covariance matrix allows constructing uncertainty intervals; it also enables testing hypothesis via a Chi-squared Wald-type test. For instance, to test whether or not $\boldsymbol{\vartheta}_{\text{veg}}$ differs significantly from another value $\boldsymbol{\vartheta}_0$, we compute the test static

$$W = \left(\hat{\boldsymbol{\vartheta}}_{\text{veg}} - \boldsymbol{\vartheta}_0\right)' \cdot \hat{\text{V}}\text{ar}^{-1} \cdot \left(\hat{\boldsymbol{\vartheta}}_{\text{veg}} - \boldsymbol{\vartheta}_0\right) \tag{16}$$

where $\hat{\boldsymbol{\vartheta}}_{\text{veg}}$ is the MLE estimate of $\boldsymbol{\vartheta}_{\text{veg}}$; both $\hat{\boldsymbol{\vartheta}}_{\text{veg}}$ and $\boldsymbol{\vartheta}_0$ are assumed to be column vectors that each comprise k elements. The statistic W has the Chi-squared distribution with a degree freedom of k, thus, allowing us to compute the p-values for the test.

3.5. Model selection for leaf angle distribution

Estimation of LAI and foliage profiles from gap or ranging data depends on which parametric model is chosen for leaf angle distribution $g(\theta)$ or $G(\theta)$. This issue is essentially a model-selection problem, which has never been resolved before but can be easily tackled by our MLE method. As summarized in Table 1, the candidate leaf angle models we considered include 15 parametric forms. Similar to model selection for multiple linear regression, we employed the Akaike information criterion (AIC) to compare the candidate models and then select the one that best matches the true leaf angle distribution for a given lidar dataset D_{lidar}. Specifically, AIC is calculated from the maximum log-likelihood (Casella and Berger, 1990):

$$\text{AIC}_i = -2\ \log\mathcal{L}\left(\hat{\boldsymbol{\vartheta}}_{\text{veg}}|D_{\text{lidar}}, G_i\right) + 2k_i \tag{17}$$

where the dependence of the likelihood $\mathcal{L}$ on the type of leaf angle distribution G_i is made explicit and $\hat{\boldsymbol{\vartheta}}_{\text{veg}}$ is the MLE estimate of $\{G\left(\theta\right), u(z)\}$ for the model type G_i. G_i is any of the candidate models in Table 1, and k_i is the number of total parameters when G_i is chosen. The best G model is chosen as the one with the smallest AIC value.

3.6. Data-specific correction for effective leaf area

Strictly speaking, the foliage density profile $u(z)$ defined and estimated above actually represents a profile of effective plant areas. $u(z)$ has to be further corrected for clumping and woody phytoelements to generate a true foliage density profile $u_t(z)$ (Chen and Cihlar, 1995):

$$u_t(z) = (1-\alpha)\frac{\gamma_e}{\Omega_e}u(z) = (1-\alpha)\frac{1}{\Omega}u(z) \tag{18}$$

where α is the nonfoliage-to-total plant area ratio; γ_e is the needle-to-shoot area ratio; and Ω_e is the clumping index synthesizing the non-random patterns of phytolements at scales larger than shoots. These factors are not explicitly accounted for by the Poisson model of Eqs. (11) and (12); therefore, α and Ω need to be estimated ad-hoc by other means. To estimate α, we clustered lidar points into 15 classes based on intensity and color RGB data via the ISO-DATA algorithm. The 15 classes were further clumped into four classes: foliage, wood, ground, and sky. The number of foliage points relative to that of woody points gives an estimate of α.

We made no further attempt to estimate Ω for correcting for clumping. As such, our final foliage density profile reported in this study is $(1-\alpha)u(z)$, which is better termed as effective foliage profile or effective LAI.

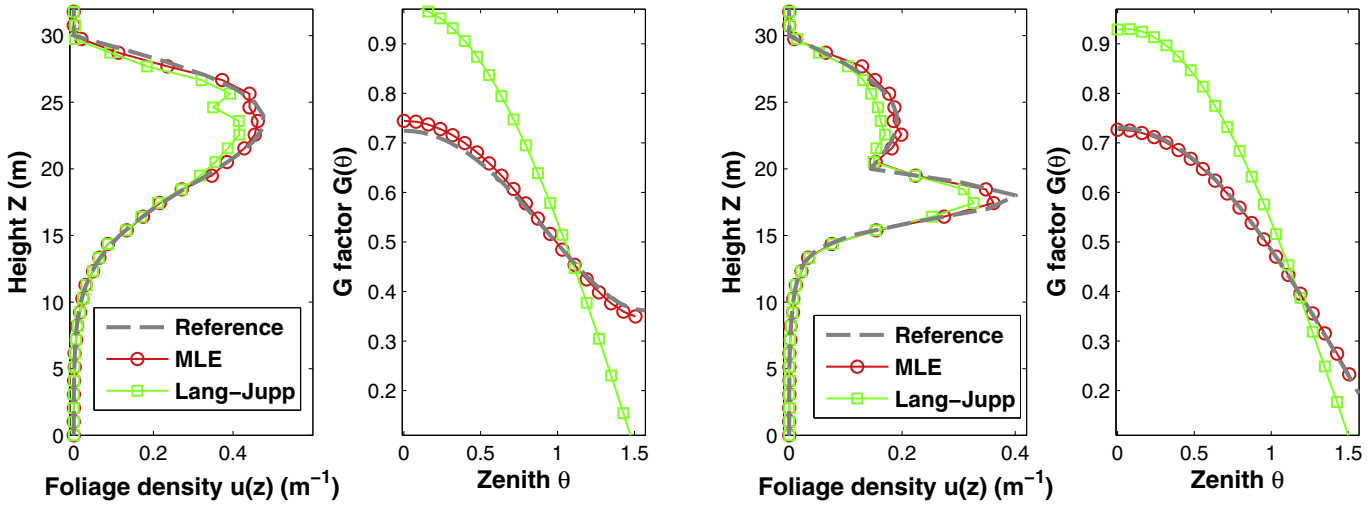

Fig. 3. MLE improved the estimation of canopy parameters over the traditional Lang–Jupp method: Foliage profiles and leaf angle distributions estimated by MLE (circle) matched the true reference (dashed line) more closely than did those by the Lang–Jupp method (square). Two examples shown here are based on simulated 3D laser data; the true reference G models chosen for the two examples are the ellipsoidal and Ross–Goudriaan's models, respectively, and the true LAI are 5.0 and 3.0, respectively.

4. Data

4.1. Simulated synthetic laser data

Both simulated and real laser data are considered for evaluating methods. Synthetic data are not just useful but necessary, simply because they seem to be the only feasible source of reliable ground-truthing for foliage profile and leaf angle distribution. Also, use of simulators permits creating consistent data for numerous plots and eliminates the influences of unknown extraneous factors. All these advantages increase the confidence in model evaluation and comparison.

To generate synthetic data, we implemented a random simulator for the Poisson model $p\left(D_{\text{lidar}}|\boldsymbol{\vartheta}_{\text{veg}}\right)$. For ease of implementation, our simulator does not consider 3D stand forests but rather horizontally-homogenous canopies. The simulator allows generating pseudo point clouds D_{lidar}, given vegetation parameters, such as foliage profile and leaf angle distribution, and the scanning configuration, such as scanner height, scanning range $r_{\max}$, the range of scanning angles, and scanning resolution. In our simulation, $G(\theta)$ was randomly selected out of the 15 candidates of Table 1; $u(z)$ was chosen as a random mixture of the Weibull, beta, and Johnson SB distributions, with canopy heights ranging from 10 m to 40 m and LAI from 0.5 to 6.5. We totally simulated 150 sets of laser ranging data emulating 150 imaginary forest plots.

4.2. Ground laser data

We also acquired four TLS scans from the online archive of the University NAVSTAR Consortium (http://tls.unavco.org/repository). The scans were conducted in April 2010 or March 2011 using a Leica ScanStation C10 instrument at four typical forest communities in Everglades National Park, USA: two upland dry habitats, pineland and hammock forests, and two wetland woody communities, cypress and mangrove forests. The pineland site has an open canopy, dominated almost exclusively by South Florida slash pine (*Pinus elliotti* var. densa). Its understory is a rich assemblage of grasses, sedges, and palm shrubs. The hammock site is a closed-canopy hardwood forest, composed dominantly of gumbo-limbo (*Bursera simaruba*), Sugarberry (*Celtis laevigata*), pigeonplum (*Coccoloba diversifolia*), and white stopper (*Eugenia axillaris*). The cypress site is a freshwater swamp forest, yet growing on poor soil and stunted also by fire; therefore, the statures of cypress trees (*Taxodium* spp.) are dwarf, generally no more than 6 m in height. The fourth site is a mangrove forest at the Shark River Slough, and the canopy is composed dominantly of red and black mangroves (*Rhizophora mangle* and *Avicennia germinans*). For all the fours scans, the laser was placed at about 2 m above the ground and was configured to scan every 0.001 rad along zenith and azimuthal directions.

5. Results

5.1. Simulated laser data

When evaluated upon the synthetic data, canopy foliage profiles were retrieved with reasonable accuracies by both the MLE and Lang–Jupp methods, but MLE outperformed the classical Lang–Jupp method. Although the foliage profiles retrieved by the two methods appeared visually similar (Fig. 3), they in many cases differed statistically (e.g., $p < 0.01$ using the W test statistic for the examples in Fig. 3). The foliage profiles estimated with MLE matched the true reference profiles more closely (e.g., $p > 0.5$ for the two examples in Fig. 3). Furthermore, the estimated LAI differed by 26% between the two methods when averaged over the 150 plots, with the MLE estimates much closer to the true LAI (Fig. 4).

In addition to foliage profiles, leaf angle distributions (LAD) were accurately estimated by the MLE method but not the Lang–Jupp method. MLE estimates of LAD were statistically indistinguishable from the true reference models for all the 150 simulated lidar plots ($p > 0.05$). As depicted in Fig. 3, the estimated G functions coincided closely with the reference ellipsoidal and Ross–Goudriaan's models ($p > 0.5$), but the estimation with the Lang–Jupp method deviated markedly from the references. More importantly, the true LAD model types—ellipsoidal and Ross–Goudriann—have been correctly identified by MLE based on AIC (Fig. 5), but these LAD distributions were not approximated well by the Jupp G model in the Lang–Jupp method (Fig. 3).

As a further evaluation of MLE for selecting LADs via AIC, we found that the LAD models have been correctly identified for 131 out of the 150 simulated plots. In the other 19 cases, the G model types with the smallest AIC values were not the true reference LADs, but the AIC values of the true model types are always the second or third smallest; their AIC values are very close to the smallest

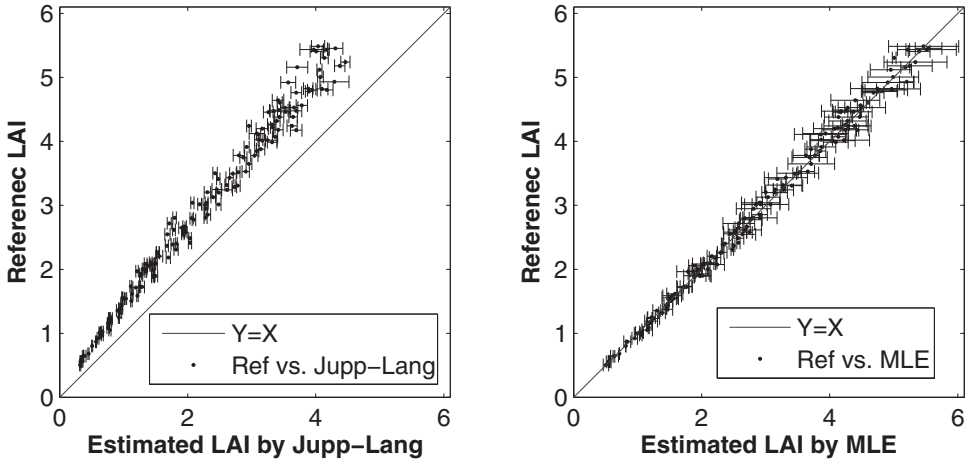

Fig. 4. Scatterplots of reference vs. estimated LAI for the Lang–Jupp method (left) and the MLE method (right). Horizontal bars indicate 95% prediction intervals.

AIC values. Such small differences in AIC suggest that the 19 misidentified G models are wrong but practically useful. Indeed, in all the 150 cases, the best G models identified were essentially the same as the corresponding true LAD ($p > 0.1$) when tested in terms of the W statistics. This statistical insignificance reveals that regardless of whether or not the true model types are chosen, the use of AIC has always found a workable model that approximated the true LAD well enough.

Error intervals were also realistically estimated by the MLE method. Alternatively speaking, estimated error intervals were indicative of the true certainties in the MLE LAI estimates, but this is not the case for the Lang–Jupp method (Fig. 4). In particular, the advantage of MLE for error analyses is demonstrated by referring to a statistic called prediction interval coverage probability (PICP). PICP quantifies how frequently prediction intervals contain true values (Zhao et al., 2013). Comparing the 95% prediction intervals against the true reference LAI, we estimated the PICP values to be 0% and 97.3% for the Lang–Jupp and MLE methods, respectively. The large deviation of 0% from its nominal value 95% indicates that the error intervals estimated by the Lang–Jupp method failed to capture the true uncertainties of LAI estimates. In contrast, the close matching between 97.3% and 95% for the MLE method highlights the usefulness of prediction intervals for characterizing the true uncertainties of MLE estimates. Furthermore, the PICP calculated based on the 65% confidence intervals is found to be 67.4% for MLE, which is close to the nominal value 65% and again suggests the effectiveness of MLE for error analyses.

5.2. Ground-based laser data

Canopy profiles estimated from the TLS data reveal large disparities in canopy structure among the four forest communities typical of Everglades National Park. The profiles all accord well with known stand characteristics (Fig. 6). The dwarf cypress forest, for example, has the lowest canopy (about 6.4 m), whereas the mangrove canopy is the highest of the four (~23.2 m). The hardwood hammock is shown to support the densest canopy, with an estimated total effective plant area of 8.76, followed by the mangrove, cypress, and pineland forests (i.e., 4.34, 1.69, and 0.57: values estimated by MLE and uncorrected for clumping). The hammock canopy profile also manifested very low foliage density near the ground, consistent with a fairly open shrub layer and a sparse, species-poor herb layer as observed in the field. The open-canopy pineland forest has the lowest estimated total leaf area; its foliage density peaks in the understory layer and was estimated to be 0.15 m^{-1} (uncorrected for clumping). This density is about twice larger than the peak foliage density observed in the upper canopy. Such a relatively thick understory corresponds to the rich assemblage of the palm shrub and other flora covers on the pineland forest floor. Between the upperstory and understory of the pineland forest is an almost open layer from the height of 2.2–9.7 m in the profile. In the cypress forest plot, the canopy profile showed a relatively large local peak in the understory, attributable mostly to cypress knees and some sawgrass cover.

The vertical canopy profiles estimated by the MLE and Lang–Jupp methods generally resembled each other (Fig. 6), both characterizing the overall forest canopy structures well. However, the profiles from the two methods also exhibited some systematic differences that were tested to be statistically significant in terms of the W statistics ($p < 0.001$). Foremost, the Lang–Jupp method yielded effective LAI smaller than the MLE estimates, a finding similar to the results from the synthetic data in Fig. 4; the relative difference averaged 61% over the four sites. Similarly, the maximum foliage densities estimated by the Lang–Jupp method were lower

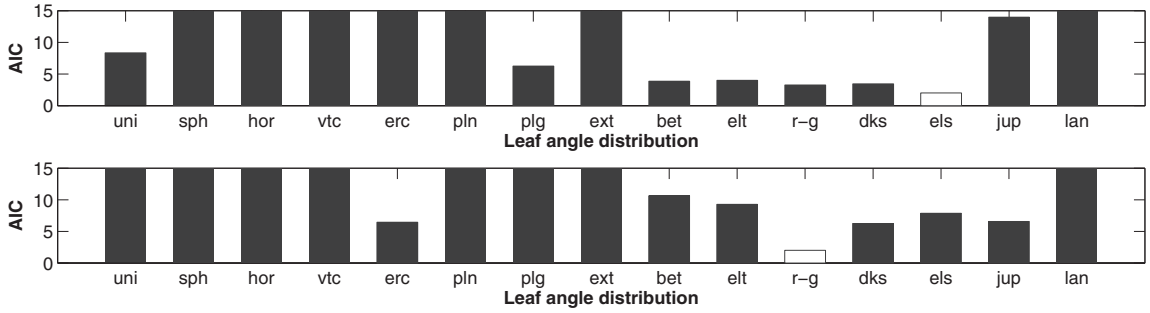

Fig. 5. Use of AIC for model selection. The true leaf angle distributions for two examples in Fig. 3 are correctly identified as those with smallest AIC values (i.e., white bars).

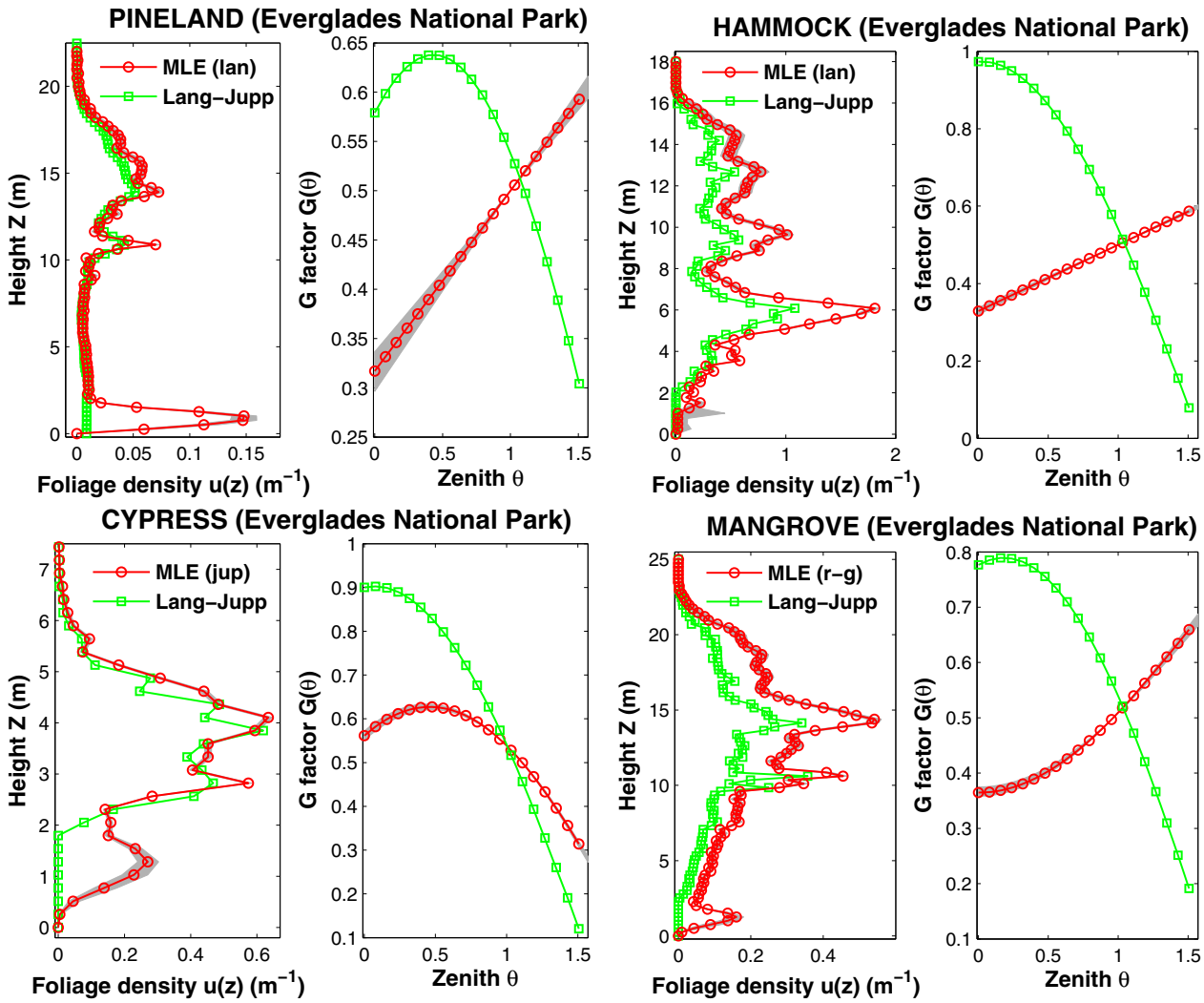

Fig. 6. Comparisons of estimated canopy parameters between the MLE (red-circle) and Lang–Jupp (green-square) methods for four sites of representative forest types in Everglades National Park, USA: Pineland, Hammock, Cypress and Mangrove. The best models of leaf angle distribution chosen by MLE were lan, lan, jup and *r*–*g* for the four sites, respectively. Gray envelopes denote 95% uncertainty intervals. (For interpretation of the references to color in this figure legend, the reader is referred to the web version of this article.)

than the MLE estimates. For example, the MLE and Lang–Jupp estimates of peak foliage density in the hammock profile was 1.8 and 1.0 m^{-1}, respectively. Of the four forests, the dwarf cypress showed the largest dissimilarity in the estimated canopy profiles between the two methods. The MLE profile of cypress exhibited three peaks, as compared to only two peaks for the Lang–Jupp method.

Estimated LADs differed markedly between the MLE and classical Lang–Jupp methods (Fig. 6). The best LADs chosen by MLE were lan for the pineland and hammock plots, jup for the cypress plot, and *r*–*g* for the mangrove plot, with the respective model parameters being 0.64, 0.66, 3, and −0.35. Their associated *G* functions depicted in Fig. 6 deviated substantially from the Lang–Jupp estimates. No ground-truthing exists to ascertain which method gave better LAD estimation. However, the MLE estimates are likely to be closer to the true LADs for the following qualitative evidence: For the mangrove forest, the MLE estimate suggests that leaves are more vertically oriented than horizontally whereas the Lang–Jupp method indicates the opposite. The MLE depiction of leaf distribution is more consistent with some field-observed ecophysiological trait of the Rhizophoraceae; that is, the more vertically leaves are oriented, the greater the salinity tolerance of the species is (Saenger, 2002).

Clustering the intensity and photography data into meaningful classes was found to be strongly sensitive to the initial parameter settings of the ISO-DATA algorithm. As a result, the use of the clustered classes to estimate wood-to-total-area ratios also varied greatly from one run of the ISO-DATA algorithm to another. For example, the nonfoliage ratio α computed for the pineland plot fell within the range of 0.05–0.43 over 50 random runs of the same clustering. Applying such ratios to correct for canopy profiles therefore will lead to large uncertainties in retrieving the true foliage profiles. Regardless of such sensitivity and uncertainty, we found that the estimated nonfoliage ratios depended strongly on height. The ratios appeared smaller for the top canopy than the bottom canopy, a pattern consistently observed for the four forest plots. For example, the estimated wood-to-total-area ratio for the upper canopy of the pineland forest (i.e., 15–20 m) was almost ten times smaller than the lower layer (i.e., 5–20 m).

6. Discussion

Tiny-footprint laser scanning resolves 3D structures of heterogeneous terrestrial environments with high precision and speed. This capability goes far beyond the proof-of-concept and was exem-

plified in earlier studies and our analyses (Jupp et al., 2009; Zheng and Moskal, 2009). The fine-grained levels of TLS data permit direct retrieval of vegetation parameters and avoid the need for auxiliary ground-truthing. The direct retrievals can be achieved using either objected-based methods to dissect point clouds (Liang et al., 2012) or physical-based model inversion such as our MLE method; the latter generally finds more use, due to the availability of physics theories to model laser–vegetation theories (Zhao et al., 2011b). However, lidar vegetation analyses are sensitive to the choices of inversion algorithms, even if using the same physics model; this sensitivity is evidenced by the 26% difference in our LAI estimates between the MLE and classical algorithms. Such a large magnitude or uncertainty, therefore, justifies our thrust for improving the use of physics for TLS vegetation analyses.

Despite the growing popularity of physically-based gap models in lidar vegetation analyses (Jupp et al., 2005), classical gap analysis methods are not tailored to TLS point cloud data (Lovell et al., 2003) and, therefore, are in many cases sub-optimal. Their weaknesses were partly overcome by our new MLE paradigm for several reasons:

(1) Classical gap methods are not optimal in terms of data use efficiency. Raw data from laser ranging or hemispheric photography do not provide direct measures of gap fractions that are needed for the classical algorithms. Rather, these gap fractions $P_{\text{gap}}\left(\theta, z\right)$ are derived beforehand from *xyz* point clouds or photos using ratio estimators. As such, the *xyz* or spherical coordinates of lidar points cannot be directly ingested in the classical formula, a weakness explicitly tackled by our MLE method.
(2) If a probability model is readily available to describe observed data, MLE comes naturally as a choice for parameter estimation from the data. Likewise, given the adopted use of the Poisson model as a probabilistic basis for TLS data, MLE is one of the most statistically justifiable choices for retrieving canopy parameters. The use of MLE not only generates the most likely values of vegetation parameters and but also provides a strict statistical framework for error analyses. In contrast, classical methods rarely permit strict error analyses with regards to the Poisson model.
(3) Classical methods usually do not allow simultaneously estimating foliage area profiles $u(z)$ and LADs $G(\theta)$. Many classical methods attempt to eliminate the influence of G functions or choose a pre-defined form for $G(\theta)$ (Jonckheere et al., 2004), but the chosen form is not guaranteed to be a realistic approximation to the true $G(\theta)$. This issue was rarely considered by classical algorithms and can be easily addressed by MLE: in addition to inferring the parameters, $G(\theta)$ and $u(z)$, MLE can compare different G model types and choose the best one among a pool of candidate LAD models.
(4) Implementations of classical methods face many practical difficulties, especially because they entail evaluating $\log P_{\text{gap}}\left(\theta, z\right)$. The observed gap fractions sometimes approaches zero at large zeniths and also exhibits substantial variability at small zenith angles, causing numerical instability and biases if not cautiously addressed (Zhao and Popescu, 2009). This difficulty or the like is not an issue for the MLE method because MLE is based on raw lidar data not gap fractions.
(5) Classical methods are not well tailored to the idiosyncrasy of TLS data. Foremost, unlike hemispheric photos that capture interactions of light with the whole canopy layer at all zenith angles and record only the silhouette of the canopy, TLS pinpoints phytoelements within a maximum radius and thus, cannot always "see" through the full canopy layer at large zenith angles beyond a critical angle (Fig. 2). As a result, the true fractions of gaps through the canopy top cannot be reliably estimated for these large angles. Also, most lidar scanners look both upward and downward. All these factors complicate the use of classical methods to handle laser scanning geometries. In contrast, our MLE method explicitly accounts for the configurations of laser scanning.

How to validate lidar estimation? Strict validation is hampered by a lack of high-fidelity ground-reference data; this is particularly true for foliage profile and LAD because they are hard to measure in-situ (Pisek et al., 2011, 2013; Wang et al., 2007). We are unaware of any existing research that directly measured stand-level canopy profiles. Rather, ground reference was often collected using indirect methods, such as point-quadrat sampling and allometric equations (Lefsky et al., 2002), but the true accuracies of such indirect ground-reference are hard to establish at first hand and could be worse than those of TLS estimates (Zhao et al., 2011a). Occasionally, accurate direct measurements are available, but a temporal or spatial discrepancy is unavoidable: The space sampled by lidar, for example, does not coincide exactly with the space of in-situ measurements (Zhao and Popescu, 2009). All these difficulties make it impractical to assess absolute accuracies of lidar-derived canopy profiles or LAD. Instead, most studies assess TLS methods only qualitatively or relative to other indirect estimates (Jupp et al., 2009). As a remedy, several studies used artificial trees with known structures (Hosoi and Omasa, 2006). Our study offered another viable alternative by using simulated data. Such well-controlled data avoided extraneous uncertainties and helped to confidently establish empirical advantages of our MLE method.

The Poisson gap model is a theoretical basis of canopy remote sensing and our MLE analyses (Nilson, 1971), but its exact model form, that we adopted is exponential rather than Poisson. This seeming discrepancy is dismissed by clarifying the assumption underlying the Poisson model: the light–vegetation interaction in one horizontal canopy layer is independent of those in other layers (Nilson, 1971, 1999). As such, the probability that a laser beam traveling along the zenith angle θ intercepts the whole canopy layer n times is a Poisson distribution $P(n) = \exp(-M)M^n/n!$ with its mean $M = G(\theta)L/\cos\theta$. Then, the probability of intercepting nothing gives the gap fraction $P(n = 0) = \exp(-G(\theta)L/\cos\theta)$, which exactly is the Poisson model of Eq. (1) and is actually an exponential distribution with respect to LAI L. Hence, the Poisson and exponential distributions are two manifestations of the same light–vegetation principle (Jonckheere et al., 2004); their associated random variables are contact number n and leaf area L, respectively. A tiny-footprint laser beam is obscured by its first interception and is unable to reliably detect the remaining contacts, if any (Zheng et al., 2013). The laser range to its first interception is a random variable compatible with cumulative leaf area, thus, making the exponential form of the Poisson model a natural choice for inference in our MLE method.

Strict use of theoretical gap models to interpret laser data is applicable for large- and tiny-footprint lidars but can be problematic for small-footprint airborne discrete-return lidar, attributed to the differing scales at which lasers interact with vegetation. In particular, a large-footprint waveform encapsulates the collective interaction of laser with leaf particles within a canopy; this scale is the traditional regime in which to apply the gap theory to build physical remote sensing models (Sun and Ranson, 2000). Hence, the Poisson model, in the form of radiative transfer theories, is applicable for analyzing large-footprint waveforms, such as ICESat/GLAS data (Koetz et al., 2006). For TLS, the tiny-footprint laser is analogous to the thin long needle as used by conventional field techniques, which captures the light–vegetation only at elements levels. But the assemblage of all laser pulses, as a whole, represents canopy-level interactions, and thus, can also be interpreted by the Poisson model, as exemplified by our MLE analysis. Contrary to large- and tiny-footprint lidars, the footprints of air-

borne lidar are incommensurate with the typical scales at which to model light–vegetation interactions. More important, airborne discrete returns are converted from raw waveform signals by some proprietary peak detection algorithms; this conversion is hard to be interpreted physically, further distorting the physical interpretation of point clouds. Zhao and Popescu (2009) explicitly discussed the theoretical dilemma caused by literally applying physically-based algorithms to analyze small-footprint discrete-return data. Overall, caution should be exercised when attempting to apply physical models to retrieve vegetation parameters from lidar data.

The theoretical applicability of MLE for TLS vegetation analyses depends on how well physical gap models describe laser–vegetation interactions captured by lidar. Therefore, as argued in the preceding paragraph, our MLE method finds better theoretical justifications for smaller laser footprints. In general, the laser footprints of commercial TLS scanners, though finite in size, are small enough to pinpoint phyto-elements (Jupp et al., 2009; Yao et al., 2011; Zhao et al., 2011a). Furthermore, although the laser spot diverges with distance, the far-field footprint sizes of many commercial TLS lidars are still relatively small; for example, Leica scanners have a nominal footprint size of <5 mm at a distance of 50 m; such a laser beam can be treated as an imaginary thin needle for intercepting phytoelements, thus justifying the validity of our MLE method. Interpreted differently, our MLE method has less theoretical justifications for those customized terrestrial lidars with relatively large footprints, such as the Echidna system with a beam size of ~50 cm at 50 m that may intercept a mixture of multiple phytoelements. However, despite this less theoretical justification, the Echidna data has been successfully inverted using gap-based algorithms (Zhao et al., 2012, 2011a); therefore, we suspect that in term of practical performances, MLE will be equally applicable for such lidar systems, which deserves further investigations.

Foliage clumping should be corrected for to derive actual leaf areas (Chen and Cihlar, 1995; Zhao et al., 2012), but our MLE method has not explicitly accounted for clumping because of some theoretical difficulty: The Poison model was originally derived for random not clumped canopies. Other two alternative gap models, binomial and Markov, have introduced some clumping indices (Nilson, 1999), but their gap formula, if treated as probability models, are not identifiable for parameter estimation. For example, the Markov gap model is $exp(-G(\theta)\Omega L(z)/\cos\theta)$, where the clumping index parameter Ω appears together with the parameter $L(z)$ in the product $\Omega L(z)$; consequentially, these two parameters are non-identifiable, an inherent difficulty that no statistical methods can tackle. This theoretical difficulty can be circumvented by at least two ways. First, an ad-hoc way is to derive the clumping index independently using some customized procedures, such as that reported in Zhao et al. (2012). Another way is to replace the Poison model in our MLE method with a complex theoretical gap model that explicitly considers canopy clumpness; one candidate is the gap model formulated in Nilson (1999).

Direct laser estimates of canopy profiles comprise both foliage and nonfoliage phytoelements. The use of TLS intensity or color data was found generally difficult, if not impossible, for correcting for non-foliage elements. For example, intensity is low because the laser beam is reflected from a target of low reflectivity or equally because it hits only part of an phytoelement. RGB photos acquired from TLS systems are of the same nature as fisheye hemispherical photos. Both the types of the photos are strongly influenced by local complex light regimes (Jonckheere et al., 2004); the varying level of shading and light-exposure within canopies complicates distinguishing between foliage and woody phytoelements from the RGB photos. To accurately derive woody-to-total area ratios, additional informative data are needed from alternative technologies. One promising option is multispectral lidar that measures spectral responses at more than on one wavelength (Gaulton et al., 2013). The multibands are often chosen purposely to maximize the spectral distinction among various scene components. Also, the use of active light sources for multispectral lidar alleviates the confounding effect of varying light levels within canopies.

Our MLE analyses emphasize not only simultaneous estimation of foliage density profile and leaf angle distribution, but also realistic error quantifications. Such uncertainty analyses were often overlooked: Although some previous studies calculated error intervals, they rarely continued to evaluate the true reliability of the estimated errors (Frazer et al., 2011; Zhao et al., 2011b). Without knowing how well the estimated errors are indicative of the true uncertainties, we cannot guarantee credible use of the estimated vegetation parameters. For this reason, we argue strongly for going beyond just estimating errors but additionally assessing the usability of the estimated errors. As exemplified here, a viable metric is PICP that allows quantifying how trustworthy the estimated uncertainties are. PICP is easy to compute without requiring additional new data; its utility has also been demonstrated in Zhao et al. (2013). The routine use of PICP therefore should be encouraged for future quantitative remote sensing applications; this practice will improve the data quality assurance of remote sensing-derived information. Overall, quantifying uncertainties is better than just ignoring them but still is not sufficient; we need to further quantify the trustworthiness of the estimated uncertainties.

Being a systematic, general-purpose inferential procedure, MLE opens up new ways to exploit gap-related remote sensing or field data for estimating LAI and LAD. In particular, MLE can be applied directly to other common gap data, such as hemispherical photos, that have been previously analyzed using classical algorithms. Our MLE paradigm can also be extended with little modifications to some troublesome scenarios difficult to tackle by classical methods, for example, when the topography is rugged or when multiple lidar scans or hemiphotos are mixed for estimation. The prior information on complex topography and the scanning geometries is attributed to individual laser pulses (Meng et al., 2010) and therefore, can be easily accounted for by MLE because the log-likelihood is formulated also at the levels of individual pulses. The exact degree to which MLE helps with these difficult scenarios should be determined in future investigations.

7. Summary

TLS or ground-based lidar becomes an increasingly valuable tool for measuring terrestrial micro-environments and holds great potential for characterizing fine-scale vegetation structures. TLS resolves tree architectures often at trunk, branch, or even leaf levels, and therefore, substantially complements airborne and spaceborne lidars for ecosystem studies. Currently, the full capability of TLS is yet to be attained, attributable partly to difficulties in data analyses. The majority of model-based TLS analyses relied on gap fractions through the use of the Poisson model as a basic theory for describing laser–vegetation interactions, but gap fractions are lidar ratio metrics reduced from raw laser ranging data, thus, leaving room to improve in terms of data use efficiency. Our MLE analyses helped to fill this critical gap by developing a strict statistical framework that directly ingests raw ranging data for estimating vegetation structural parameters.

As a flexible physically-based algorithm for retrieving biophysical variables, our MLE framework is theoretically justifiable, conceptually simple, and practically effective. Compared to classical methods, MLE accommodates the idiosyncrasy of laser scanning geometry and data characteristic, capitalizes on more information inherent in lidar data, and improves laser-based characterization of canopy vertical structure. Additionally, MLE tackles uncertainty analyses explicitly and realistically, an aspect that is critical but was largely overlooked. Evaluations of the methods suggest that

the MLE estimates of foliage profiles and leaf angle distributions differed from the estimation using the classical method, often to a statistically significant degree. When tested upon synthetic data, MLE outcompeted the classical estimation. The combination of theoretical and experiment evidence confirmed that MLE is a paradigm-shifting method for exploring laser ranging data and it enhances the capability of terrestrial lidar for characterizing forest canopies. The MLE method also has good generality and can be applied to analyze other gap and ranging data, such as hemispherical photos and airborne laser data, with no or little modification. Such extended applications should be examined in future research. Overall, high-precision lidar measurements, in conjunction with advanced data analyses as developed here, delivers reliable vegetation information to improve understandings of ecosystem structure and functioning.

Acknowledgements

This work was supported by a start-up fund from the Ohio State University, a China Scholar Council fellowship "201406170122", a NASA new investigator award "13-NIP13-0046", and the NASA ROSES LULC Program "NNH11ZDA001N-LCLUC". This work was also supported in part by an allocation of computing time from the Ohio Supercomputer Center. We thank Mr. Sheng Nie and Drs. Mark Danson, Demetrios Gatziolis, Ross Nelson, Bruce Cook, Yong Pang, and Wenjie Fang for helpful discussion or useful comments. We are also indebted to the two anonymous reviewers for their valuable comments.

Appendix A.

1. Leaf angle distribution and Ross–Nilson G function

The leaf angle distribution $g(\theta)$ is a probability density over the upper hemisphere, which satisfies $\int_0^{\pi/2} g(\theta)\sin\theta \mathrm{d}\theta = 1$. More important, for a canopy, its leaf angle distribution $g(\theta)$ fully determines the associated Ross–Nilson G function, following the relationship (Wang et al., 2007; Wilson, 1960):

$$\begin{aligned} G(\theta) &= \frac{1}{2\pi}\int_0^{2\pi}\mathrm{d}\varphi\int_0^{\pi/2} g(\theta')|\cos\theta\cdot\cos\theta' + \sin\theta\cdot\sin\theta'|\sin\theta\mathrm{d}\theta' \\ &= \int_0^{\pi/2} g(\theta')\underline{\underline{S(\theta',\theta)}}\,\mathrm{d}\theta' \\ \underline{\underline{S(\theta',\theta)}} &= \begin{cases} \dfrac{|\cos\theta\cdot\cos\theta'|}{\cos\theta\cdot\cos\theta'\cdot\left(\dfrac{2\widetilde{\varphi_t}}{\pi}-1\right)+\dfrac{2}{\pi}\sin\theta\sin\theta'\sin\widetilde{\varphi_t}} & \begin{array}{l}\text{if}|\cos\theta\cos\theta'|\geq 1\\ \text{otherwise}\end{array} \end{cases} \\ \widetilde{\varphi_t} &= \arccos(-\cot\theta\cdot\cos\theta'). \end{aligned} \tag{A1}$$

2. Simple justifications for MLE

The following toy example is given to help non-expert readers to quickly grasp the essence of our MLE method and understand why MLE is preferred to classical gap-based methods for analyzing laser ranging data. Specifically, consider a probability model $p(z|\vartheta) = \vartheta\exp(-\vartheta z)$ for laser ranging z with the true parameter being $\vartheta = 0.1$, from which we generated 10 random ranging observations of z: $D = [16.5, 18.5, 11.2, 5.5, 8.4, 1.0, 11.3, 22.4, 5.5, \text{and } 1.1]$. To estimate ϑ from D, the classical gap method does not directly use the original ranging-based model $p(z|\vartheta)$ but turns to an equivalent gap-based model $P_{\text{gap}}(z|\vartheta) = 1 - \int_0^z p(z'|\vartheta)\,\mathrm{d}z' = \exp(-\vartheta z)$, which gives

$$\hat{\vartheta}_{\text{gap}} = \frac{-\log\left(\hat{P}_{\text{gap}}(z|\vartheta)\right)}{z}. \tag{A2}$$

If z is taken to be 10.0, then five out of the ten observed z's in D are beyond z, giving an estimated gap of $\hat{P}_{\text{gap}}(z|\vartheta) = \frac{5}{10} = .5$. We thus get an estimate $\hat{\vartheta}_{\text{gap}} = -\log(.5)/10 = 0.069$, as compared to the true value $\vartheta = 0.1$.

In contrast, MLE directly deals with the ranging data and it finds the best ϑ by maximizing the likelihood:

$$\hat{\vartheta}_{\text{MLE}} = \text{argmax}_\vartheta\, p(D|\vartheta) = \text{argmax}_\vartheta\, p(16.5|\vartheta)\,p(18.5|\vartheta)\cdots p(1.1|\vartheta) \tag{A3}$$

which gives $\hat{\vartheta}_{\text{MLE}} = 0.099$ with a 95% confidence interval [0.04, 0.16]. This estimate is very close to the true value 0.1 and it also falls into the estimated interval. Overall, MLE provides a strict framework for statistical inference and uncertainty analyses.

This example, though simple and contrived, captures the essence of our MLE method. We further expounded on it to show how MLE improves upon data use efficiency. By comparison, MLE uses the original data D but the gap method $\hat{\vartheta}_{\text{gap}}$ relies on only the ratio (i.e., $\frac{5}{10} = 0.5$). The use of the ratio (i.e., 0.5) loses much information in the raw data because it is impossible to recover the z's from only 0.5. Also, the same ratio value can be obtained by using any z threshold between 8.4 and 11.2, thereby contributing some artificial variability to the estimated $\hat{\vartheta}_{\text{gap}}$. Furthermore, the ratio by itself bears no information on the because the ratio 0.5 can be equally obtained from 1/2, 2/4, 4/8, or 10/20, among others. Statistically speaking, this loss of the information about the numbers of observations renders it impossible to estimate the uncertainty associated with the classical estimate $\hat{\vartheta}_{\text{gap}}$.

3. Numerical implementation of MLE

Use of MLE to estimate vegetation parameters $\boldsymbol{\vartheta}_{\text{veg}}$ based on the Poisson model $p\left(D_{\text{lidar}}|\boldsymbol{\vartheta}_{\text{veg}}\right)$ is conceptually simple, but its implementation has to tackle some practical challenges.

First and foremost, unlike LAI being a scalar, the parameters of our model, $\boldsymbol{\vartheta}_{\text{veg}} = \left\{L(z), G(\theta)\right\}$, are functions by themselves. As explained in Section 3.3, we chose to consider parametric and non-parametric forms for leaf angle distribution $G(\theta)$ and foliage density profile $u(z)$, respectively. In particular, $G(\theta)$ is specified by a pre-defined equation together with its associated parameters χ, as denoted by $G\left(\theta;\chi\right)$ (Table 1). The estimation of the whole function $G(\theta)$ then reduces to only estimating its parameters χ. In contrast, leaf area density $u(z)$ is chosen to be discretized and represented by its values at a list of consecutive heights $u(z) = \{u_j\}_{j=1,\ldots,m}$ (Zhao et al., 2009). Accordingly, the parameters to be optimized become $\boldsymbol{\vartheta}_{\text{veg}} = [\chi; u_1, u_2, \ldots, u_m]$, but this discretized version of $u(z)$ sometimes results in hundreds of scalars, rendering the optimization problem numerically ill-posed and the MLE estimation of $u(z)$ unstable. To suppress this ill-posedness, we employed a regularization method by introducing a penalty term to control the smoothness of the discretized foliage profile $u(z) = \{u_j\}_{j=1,\ldots,m}$ (Hansen, 1999). The particular penalty we choose is the integral of squared differential of $u(z)$, which leads to a penalized log-likelihood function:

$$\begin{aligned} \mathcal{L}_{\text{pen}}\left(G\left(\theta\right), u(z)|D_{\text{lidar}}\right) &= \log p\left(D_{\text{lidar}}|G\left(\theta\right), u(z)\right) \\ &\quad + \lambda.\int\left(\frac{\mathrm{d}u}{\mathrm{d}z}\right)^2\mathrm{d}z \end{aligned} \tag{A4}$$

where λ is a positive regularization parameter. A larger λ will lead to a smoother estimate of $u(z)$. Our implemented MLE estimator is to find those values, $\hat{\boldsymbol{\vartheta}}_{\text{MLE}} = \left[\hat{\chi}; \hat{u}_1, \hat{u}_2, \ldots, \hat{u}_m\right]$, that maximize the penalized likelihood $\mathcal{L}_{\text{pen}}(\boldsymbol{\vartheta}_{\text{veg}} = \{G(\theta), u(z)\}|D_{\text{lidar}})$.

Second, another issue concerns tuning the smoothing parameters λ. Although λ itself is of no inferential interest, the choice

of λ matters. In the penalized likelihood of Eq. (A4), λ controls the weight given to the minimization of the roughness penalty term relative to the minimization of the negative log-likelihood term. A larger λ gives a smoother estimate of foliage profile $\hat{u}_{\mathrm{MLE}}(z) = \left[\hat{u}_1, \hat{u}_2, \ldots, \hat{u}_m\right]$. Many tools and criteria, such as generalized cross-validation and generalized information criterion, have been suggested for guiding selection of the regularization parameter (Konishi and Kitagawa, 1996; Ueki and Fueda, 2010). The particular method we chose is a well-known technique called the "*L*-curve" method (Hansen, 1999). The *L*-curve refers to the plotting of the negative log-likelihood vs. the roughness penalty (i.e., $\log p\left(D_{\mathrm{lidar}}|\hat{G}_{\mathrm{MLE}}\left(\theta\right), \hat{u}_{\mathrm{MLE}}(z)\right)$ vs. $\int\left(\mathrm{d}\hat{u}_{\mathrm{MLE}}(z)/\mathrm{d}z\right)^2\mathrm{d}z$), calculated for a series of values of λ. This curve always shows a characteristic L shape. No choices of λ can give a solution that corresponds to a point below the *L*-curve; therefore, a good value of λ is chosen as the one corresponding to the corner of the *L* curve, which can be obtained as the position with the largest curvature. This choice represents a good compromise between the two minimization terms, as has been widely adopted.

Third, the optimization involved for maximizing the penalized likelihood is a constrained problem because of the constraints on the range of vegetation parameters. For example, the χ_L parameter in the Dickinson's leaf angle distribution model falls into [−1, 1]; values of foliage density $\{u_j\}_{j=1,\ldots,m}$ have to be non-negative. These constraints preclude direct use of fast unconstrained optimizers. Although many constrained optimizers are available to account for these range constraints, our preliminary trials with some of them (i.e., the interior point, active-set, and sequential quadratic programming algorithms) suggested that the constrained algorithms are too computationally demanding to be effective choices for our MLE method (e.g., often with a computation cost of ∼10 h for a typical ground-lidar scan). As a remedy, we converted the original constrained MLE problem in Eq. (A2) to an unconstrained one by applying the trick of variable transformation. Specifically, we transformed a variable x bounded within $[a, b]$ to a boundless variable t (i.e., $t \in (-\infty, \infty)$) using

$$t = \log\frac{x-a}{b-x}; x \in (a, b) \tag{A5}$$

This transformation helps to convert the original vegetation parameters $\boldsymbol{\vartheta}_{\mathrm{veg}} = [\chi; u_1, u_2, \ldots, u_m]$ to a set of boundless parameters $[t; w_1, w_2, \ldots, w_m]$, with regards to some meaningfully chosen bounds a and b. The new parameterization then allows us to apply a very efficient gradient-based unconstrained optimizer, namely, the Polak–Ribière nonlinear conjugate gradient algorithm, to find the MLE estimate $\left[\hat{t}; \hat{w}_1, \hat{w}_2, \ldots, \hat{w}_m\right]_{\mathrm{MLE}}$. The iterative searching for this algorithm is based on gradients, such as $\partial\mathcal{L}_{\mathrm{pen}}/\partial t$, and $\partial\mathcal{L}_{\mathrm{pen}}/\partial\omega$, that are not always analytically available, and thus, are numerically evaluated when necessary. The MLE estimate $\left[\hat{t}; \hat{w}_1, \hat{w}_2, \ldots, \hat{w}_m\right]_{\mathrm{MLE}}$ is in the transformed scale and needs to be back-transformed to the original scale using the following equation:

$$x = \frac{(b-a)\times\exp(t)}{1+\exp(t)} + a; t \in (-\infty, \infty) \tag{A6}$$

which leads to the final MLE estimate of vegetation parameters $\hat{\vartheta}_{\mathrm{MLE}} = \left[\hat{\chi}; \hat{u}_1, \hat{u}_2, \ldots, \hat{u}_m\right]$. The use of this unconstrained scheme greatly speeded up the optimization and, when tested upon our ground-laser scans, often took less than a few minutes.

Fourth, the use of the conjugate gradient optimizer tends to render our MLE estimate sensitive to the choice of initial value. This weakness is inherent to all gradient-based optimizers, especially for high-dimensional problems. No universal rules exist to avoid trapping into local minima/maxima. One remedy is to choose an initial value close to the true solution. Another one is to run the optimization multiple times from different initial values and then choose the best run (Zhao et al., 2008). We applied both the strategies. Specifically, we took advantage of the classical Lang–Jupp algorithm and used it to generate informative initial values for $u(z)$. For the Ross–Nilson function $G\left(\theta; \chi\right)$, we chose ten random initial values for χ and correspondingly estimated the MLE ten times to choose the best one.

References

Campbell, G., Norman, J., 1989. The description and measurement of plant canopy structure. In: Plant Canopies: Their Growth, Form and Function. Cambridge University Press, pp. 1–19.

Casella, G., Berger, R.L., 1990. Statistical Inference. Duxbury Press Belmont, CA.

Chen, G., Hay, G.J., 2011. A support vector regression approach to estimate forest biophysical parameters at the object level using airborne lidar transects and Quickbird data. Photogramm. Eng. Remote Sens. 77, 733–741.

Chen, J.M., Cihlar, J., 1995. Quantifying the effect of canopy architecture on optical measurements of leaf area index using two gap size analysis methods. Geosci. Remote Sens. IEEE Trans. 33, 777–787.

Chen, Q., Baldocchi, D., Gong, P., Dawson, T., 2008. Modeling radiation and photosynthesis of a heterogeneous savanna woodland landscape with a hierarchy of model complexities. Agric. For. Meteorol. 148, 1005–1020.

Dalponte, M., Bruzzone, L., Gianelle, D., 2011. A system for the estimation of single-tree stem diameter and volume using multireturn LIDAR data. Geosci. Remote Sens. IEEE Trans. 49, 2479–2490.

Frazer, G., Magnussen, S., Wulder, M., Niemann, K., 2011. Simulated impact of sample plot size and co-registration error on the accuracy and uncertainty of LiDAR-derived estimates of forest stand biomass. Remote Sens. Environ. 115, 636–649.

García, M., Popescu, S., Riaño, D., Zhao, K., Neuenschwander, A., Agca, M., Chuvieco, E., 2012. Characterization of canopy fuels using ICESat/GLAS data. Remote Sens. Environ. 123, 81–89.

Gaulton, R., Danson, F., Ramirez, F., Gunawan, O., 2013. The potential of dual-wavelength laser scanning for estimating vegetation moisture content. Remote Sens. Environ. 132, 32–39.

Hansen, P.C., 1999. The *L*-Curve and Its Use in the Numerical Treatment of Inverse Problems. IMM, Department of Mathematical Modelling, Technical University of Denmark.

Hosoi, F., Nakai, Y., Omasa, K., 2013. 3-D voxel-based solid modeling of a broad-leaved tree for accurate volume estimation using portable scanning lidar. ISPRS J. Photogramm. Remote Sens. 82, 41–48.

Hosoi, F., Omasa, K., 2006. Voxel-based 3-D modeling of individual trees for estimating leaf area density using high-resolution portable scanning lidar. Geosci. Remote Sens. IEEE Trans. 44, 3610–3618.

Hurtt, G.C., Dubayah, R., Drake, J., Moorcroft, P.R., Pacala, S.W., Blair, J.B., Fearon, M.G., 2004. Beyond potential vegetation: combining lidar data and a height-structured model for carbon studies. Ecol. Appl. 14, 873–883.

Jakubowski, M.K., Guo, Q., Kelly, M., 2013. Tradeoffs between lidar pulse density and forest measurement accuracy. Remote Sens. Environ. 130, 245–253.

Jonckheere, I., Fleck, S., Nackaerts, K., Muys, B., Coppin, P., Weiss, M., Baret, F., 2004. Review of methods for in situ leaf area index determination: Part I. Theories: sensors and hemispherical photography. Agric. For. Meteorol. 121, 19–35.

Jupp, D.L., Culvenor, D., Lovell, J., Newnham, G., Strahler, A., Woodcock, C., 2009. Estimating forest LAI profiles and structural parameters using a ground-based laser called 'Echidna®'. Tree Physiol. 29, 171–181.

Jupp, D.L., Culvenor, D., Lovell, J.L., Newnham, G., 2005. Evaluation and Validation of Canopy Laser Radar (LIDAR) Systems for Native and Plantation Forest Inventory. Final Report Prepared for the Forest and Wood Products Research and Development Corporation (FWPRDC: PN 02.2902) by CSIRO, 20, 150.

Koetz, B., Morsdorf, F., Sun, G., Ranson, K., Itten, K., Allgower, B., 2006. Inversion of a lidar waveform model for forest biophysical parameter estimation. Geosci. Remote Sens. Lett. IEEE 3, 49–53.

Konishi, S., Kitagawa, G., 1996. Generalised information criteria in model selection. Biometrika 83, 875–890.

Lang, A., 1987. Simplified estimate of leaf area index from transmittance of the sun's beam. Agric. For. Meteorol. 41, 179–186.

Lefsky, M.A., Cohen, W.B., Parker, G.G., Harding, D.J., 2002. Lidar remote sensing for ecosystem studies: lidar, an emerging remote sensing technology that directly measures the three-dimensional distribution of plant canopies, can accurately estimate vegetation structural attributes and should be of particular interest to forest, landscape, and global ecologists. BioScience 52, 19–30.

Liang, X., Litkey, P., Hyyppa, J., Kaartinen, H., Vastaranta, M., Holopainen, M., 2012. Automatic stem mapping using single-scan terrestrial laser scanning. Geosci. Remote Sens. IEEE Trans. 50, 661–670.

Liang, X.L., Hyyppa, J., 2013. Automatic stem mapping by merging several terrestrial laser scans at the feature and decision levels. Sensors 13, 1614–1634.

Lin, Y., Hyyppa, J., Jaakkola, A., 2011. Mini-UAV-borne LIDAR for fine-scale mapping. Geosci. Remote Sens. Lett. IEEE 8, 426–430.

Lovell, J., Jupp, D.L., Culvenor, D., Coops, N., 2003. Using airborne and ground-based ranging lidar to measure canopy structure in Australian forests. Can. J. Remote Sens. 29, 607–622.

Medhurst, J.L., Beadle, C.L., 2001. Crown structure and leaf area index development in thinned and unthinned *Eucalyptus nitens* plantations. Tree Physiol. 21, 989–999.

Meng, X., Currit, N., Zhao, K., 2010. Ground filtering algorithms for airborne LiDAR data: a review of critical issues. Remote Sens. 2, 833–860.
Mori, S., Hagihara, A., 1991. Crown profile of foliage area characterized with the weibull distribution in a Hinoki (*Chamaecyparis obtusa*) stand. Trees Struct. Funct. 5, 149–152.
Mutlu, M., Popescu, S.C., Zhao, K., 2008. Sensitivity analysis of fire behavior modeling with LIDAR-derived surface fuel maps. For. Ecol. Manage. 256, 289–294.
Myung, I.J., 2003. Tutorial on maximum likelihood estimation. J. Math. Psychol. 47, 90–100.
Ni-Meister, W., Strahler, A.H., Woodcock, C.E., Schaaf, C.B., Jupp, D.L., Yao, T., Zhao, F., Yang, X., 2008. Modeling the hemispherical scanning: below-canopy lidar and vegetation structure characteristics with a geometric-optical and radiative-transfer model. Can. J. Remote Sens. 34, S385–S397.
Nilson, T., 1971. A theoretical analysis of the frequency of gaps in plant stands. Agric. Meteorol. 8, 25–38.
Nilson, T., 1999. Inversion of gap frequency data in forest stands. Agric. For. Meteorol. 98, 437–448.
Otto, S., Trautmann, T., 2008. A note on G-functions within the scope of radiative transfer in turbid vegetation media. J. Quant. Spectrosc. Radiat. Transf. 109, 2813–2819.
Palace, M.W., Sullivan, F.B., Ducey, M.J., Treuhaft, R.N., Herrick, C., Shimbo, J.Z., Mota-E-Silva, J., 2015. Estimating forest structure in a tropical forest using field measurements, a synthetic model and discrete return lidar data. Remote Sens. Environ. 161, 1–11.
Pisek, J., Ryu, Y., Alikas, K., 2011. Estimating leaf inclination and G-function from leveled digital camera photography in broadleaf canopies. Trees 25, 919–924.
Pisek, J., Sonnentag, O., Richardson, A.D., Mõttus, M., 2013. Is the spherical leaf inclination angle distribution a valid assumption for temperate and boreal broadleaf tree species? Agric. For. Meteorol. 169, 186–194.
Popescu, S.C., Zhao, K., 2008. A voxel-based lidar method for estimating crown base height for deciduous and pine trees. Remote Sens. Environ. 112, 767–781.
Popescu, S.C., Zhao, K., Neuenschwander, A., Lin, C., 2011. Satellite lidar vs: small footprint airborne lidar: comparing the accuracy of aboveground biomass estimates and forest structure metrics at footprint level. Remote Sens. Environ. 115, 2786–2797.
Rich, P.M., Wood, J., Vieglais, D., Burek, K., Webb, N., 1999. HemiView User Manual, Version 2.1. Delta-T Devices Ltd., Cambridge, UK, pp. 79.
Richardson, J.J., Moskal, L.M., Kim, S.-H., 2009. Modeling approaches to estimate effective leaf area index from aerial discrete-return LIDAR. Agric. For. Meteorol. 149, 1152–1160.
Saenger, P., 2002. Mangrove Ecology, Silviculture and Conservation. Springer.
Sun, G., Ranson, K.J., 2000. Modeling lidar returns from forest canopies. Geosci. Remote Sens. IEEE Trans. 38, 2617–2626.
Tang, H., Brolly, M., Zhao, F., Strahler, A.H., Schaaf, C.L., Ganguly, S., Zhang, G., Dubayah, R., 2014. Deriving and validating leaf area index (LAI) at multiple spatial scales through lidar remote sensing: a case study in Sierra National Forest, CA. Remote Sens. Environ. 143, 131–141.
Ueki, M., Fueda, K., 2010. Optimal tuning parameter estimation in maximum penalized likelihood method. Ann. Inst. Stat. Math. 62, 413–438.
van Aardt, J.A., Wynne, R.H., Oderwald, R.G., 2006. Forest volume and biomass estimation using small-footprint lidar-distributional parameters on a per-segment basis. For. Sci. 52, 636–649.
Vierling, K.T., Vierling, L.A., Gould, W.A., Martinuzzi, S., Clawges, R.M., 2008. Lidar: shedding new light on habitat characterization and modeling. Front. Ecol. Environ. 6, 90–98.
Wang, W.-M., Li, Z.-L., Su, H.-B., 2007. Comparison of leaf angle distribution functions: effects on extinction coefficient and fraction of sunlit foliage. Agric. For. Meteorol. 143, 106–122.
Wilson, J.W., 1960. Inclined point quadrats. New Phytol. 59, 1–7.
Woodgate, W., Jones, S.D., Suarez, L., Hill, M.J., Armston, J.D., Wilkes, P., Soto-Berelov, M., Haywood, A., Mellor, A., 2015. Understanding the variability in ground-based methods for retrieving canopy openness, gap fraction: and leaf area index in diverse forest systems. Agric. For. Meteorol. 205, 83–95.
Yang, X.S., Miller, D.R., Montgomery, M.E., 1993. Vertical distributions of canopy foliage and biologically-active radiation in a defoliated/refoliated hardwood forest. Agric. For. Meteorol. 67, 129–146.
Yao, T., Yang, X., Zhao, F., Wang, Z., Zhang, Q., Jupp, D., Lovell, J., Culvenor, D., Newnham, G., Ni-Meister, W., 2011. Measuring forest structure and biomass in New England forest stands using Echidna ground-based lidar. Remote Sens. Environ. 115, 2965–2974.
Yu, X., Hyyppä, J., Vastaranta, M., Holopainen, M., Viitala, R., 2011. Predicting individual tree attributes from airborne laser point clouds based on the random forests technique. ISPRS J. Photogramm. Remote Sens. 66, 28–37.
Zellweger, F., Morsdorf, F., Purves, R.S., Braunisch, V., Bollmann, K., 2014. Improved methods for measuring forest landscape structure: LiDAR complements field-based habitat assessment. Biodivers. Conserv. 23, 289–307.
Zhao, F., Strahler, A.H., Schaaf, C.L., Yao, T., Yang, X., Wang, Z., Schull, M.A., Román, M.O., Woodcock, C.E., Olofsson, P., 2012. Measuring gap fraction: element clumping index and LAI in Sierra Forest stands using a full-waveform ground-based lidar. Remote Sens. Environ. 125, 73–79.
Zhao, F., Yang, X., Schull, M.A., Román-Colón, M.O., Yao, T., Wang, Z., Zhang, Q., Jupp, D.L., Lovell, J.L., Culvenor, D.S., 2011a. Measuring effective leaf area index, foliage profile: and stand height in New England forest stands using a full-waveform ground-based lidar. Remote Sens. Environ. 115, 2954–2964.
Zhao, K., Jackson, R.B., 2014. Biophysical forcings of land-use changes from potential forestry activities in North America. Ecol. Monogr. 84, 329–353.
Zhao, K., Popescu, S., 2009. Lidar-based mapping of leaf area index and its use for validating GLOBCARBON satellite LAI product in a temperate forest of the southern USA. Remote Sens. Environ. 113, 1628–1645.
Zhao, K., Popescu, S., Meng, X., Pang, Y., Agca, M., 2011b. Characterizing forest canopy structure with lidar composite metrics and machine learning. Remote Sens. Environ. 115, 1978–1996.
Zhao, K., Popescu, S., Nelson, R., 2009. Lidar remote sensing of forest biomass: a scale-invariant estimation approach using airborne lasers. Remote Sens. Environ. 113, 182–196.
Zhao, K., Popescu, S., Zhang, X., 2008. Bayesian learning with Gaussian processes for supervised classification of hyperspectral data. Photogramm. Eng. Remote Sens. 74, 1223–1234.
Zhao, K., Valle, D., Popescu, S., Zhang, X., Mallick, B., 2013. Hyperspectral remote sensing of plant biochemistry using Bayesian model averaging with variable and band selection. Remote Sens. Environ. 132, 102–119.
Zheng, G., Moskal, L.M., 2009. Retrieving leaf area index (LAI) using remote sensing: theories, methods and sensors. Sensors 9, 2719–2745.
Zheng, G., Moskal, L.M., Kim, S.-H., 2013. Retrieval of effective leaf area index in heterogeneous forests with terrestrial laser scanning. Geosci. Remote Sens. IEEE Trans. 51 (2), 777–786.